Neoplasia • Vol. 8, No. 4, April 2006, pp. 302–311 302

www.neoplasia.com

Fluorescent Nanoparticle Uptake for Brain Tumor Visualization[1]

Rachel Tréhin, Jose-Luiz Figueiredo, Mikael J. Pittet[2], Ralph Weissleder, Lee Josephson and Umar Mahmood

Center for Molecular Imaging Research, Massachusetts General Hospital, Harvard Medical School, Charlestown, MA 02129, USA

Abstract

Accurate delineation of tumor margins is vital to the successful surgical resection of brain tumors. We have previously developed a multimodal nanoparticle CLIO-Cy5.5, which is detectable by both magnetic resonance imaging and fluorescence, to assist in intraoperatively visualizing tumor boundaries. Here we examined the accuracy of tumor margin determination of orthotopic tumors implanted in hosts with differing immune responses to the tumor. Using a nonuser-based signal intensity method applied to fluorescent micrographs of 9L gliosarcoma green fluorescent protein (GFP) tumors, mean overestimations of 2 and 24 μm were obtained using Cy5.5 fluorescence, compared to the true tumor margin determined by GFP fluorescence, in nude mice and rats, respectively. To resolve which cells internalized the nanoparticle and to quantitate degree of uptake, tumors were disaggregated and cells were analyzed by flow cytometry and fluorescence microscopy. Nanoparticle uptake was seen in both $CD11b^+$ cells (representing activated microglia and macrophages) and tumor cells in both animal models by both methods. $CD11b^+$ cells were predominantly found at the tumor margin in both hosts, but were more pronounced at the margin in the rat model. Additional metastatic (CT26 colon) and primary (Gli36 glioma) brain tumor models likewise demonstrated that the nanoparticle was internalized both by tumor cells and by host cells. Together, these observations suggest that fluorescent nanoparticles provide an accurate method of tumor margin estimation based on a combination of tumor cell and host cell uptake for primary and metastatic tumors in animal model systems and offer potential for clinical translation.

Neoplasia (2006) **8,** 302–311

Keywords: Brain tumor, optical imaging, nanoparticle, fluorescence, MRI.

Introduction

Completeness of resection has been correlated with improved survival in studies of various brain tumor populations [1,2]. Accurate brain tumor delineation is a challenging task that is crucial to improving the degree of resection while preserving normal tissues. Over the years, a variety of optical agents have been employed to improve this process. The low-molecular-weight fluorochrome fluorescein was employed more than 50 years ago to assess whether it could help differentiate gliomas from normal brain during biopsy [3]. More recently, indocyanine green was evaluated for its ability to enhance tumor boundaries [4,5]. Although these fluorochromes provide intraoperative fluorescence in the region of the tumor, they have not been widely accepted as providing accurate margin delineation. These small molecules have limited circulation time and readily diffuse into and out of the interstitial space. A similar pharmacokinetic pattern is obtained with low-molecular-weight gadolinium chelates, which are administered minutes before contrast-enhanced magnetic resonance imaging (MRI) is obtained and do not remain in the same distribution over the hours required for tumor resection. Washout and diffusion of such agents progressively decrease contrast enhancement.

We recently developed a nanoparticle CLIO-Cy5.5, which is both an MRI contrast agent and a near-infrared fluorescent optical probe [6]. CLIO-Cy5.5 is composed of a superparamagnetic iron oxide core coated with crosslinked dextran to which the fluorochrome Cy5.5 is covalently attached. The nanoparticle has significant advantages over previously used optical agents in terms of brain tumor delineation. Unlike low-molecular-weight fluorescent dyes or gadolinium chelates, the nanoparticle is internalized by cells before surgery commences and does not diffuse out of cells or through the interstitial space during surgery. A comparison of long *versus* short circulating iron oxides used clinically showed that only the long circulating nanoparticles accumulated in human brain tumors [7]. MION, the parent nanoparticle of CLIO, has a blood half-life of about 24 hours in humans [8], whereas MION and the amino-CLIO nanoparticle have a blood half-life of 10 hours in mice [9]. Long circulating magnetic nanoparticles may be useful for visualizing some blood–brain barrier disruptions that are not detected by standard gadolinium-enhanced MRI in human infarcts [10] or with some brain tumor metastatic foci [7]. Over a period of 3 to 7 days, the iron of injected superparamagnetic iron oxides is degraded and used [11]. Thus, long circulating nanoparticles

Address all correspondence to: Umar Mahmood, MD, PhD, Center for Molecular Imaging Research, Massachusetts General Hospital, Harvard Medical School, Building 149, 13th Street, No. 5408, Charlestown, MA 02129. E-mail: mahmood@helix.mgh.harvard.edu

[1]This work was supported, in part, by National Institutes of Health grant EB001872 and by P50 C 86355. R.T. was supported by stipend from the Swiss National Foundation.

[2]M.P. was supported by Human Frontier Science Program Organization LT00369/2003.

DOI 10.1593/neo.05751

slowly accumulate in brain tumors, but are even more slowly degraded, yielding a window of approximately 12 to 48 hours postinjection when they are trapped inside cells and can be used to visualize tumor margins. In addition, regions of intraoperative fluorescence can be directly compared with regions of nanoparticle-induced signal loss seen on preoperative MR images. Moreover, the use of a near-infrared fluorochrome (Cy5.5) provides both markedly improved light transmission through tissues [12] and decreased autofluorescence compared to fluorescein or other visible wavelength-emitting fluorochromes. Finally, near-infrared emission permits simultaneous full-color spectrum white light imaging while acquiring and displaying fluorescence separately [13], allowing real-time fluorescence-based updates of resected tumor margins without sacrificing color-based cues.

We previously employed the CLIO-Cy5.5 nanoparticle to delineate brain tumor margins in a rat model using a 9L gliosarcoma that is stably transfected to express green fluorescent protein (GFP) [6]. The goals of the present study were as follows: 1) to examine nanoparticle-based margin delineation with the 9L gliosarcoma cell line implanted in hosts with differing immune responses to the tumor (immunocompetent rats and nude mice); 2) to use a predefined signal intensity–based quantitative method to define tumor margins with fluorescent micrographs, and to assess the accuracy of margin delineation; 3) to determine which cells internalize the CLIO-Cy5.5 nanoparticle by disaggregation of the tumors of injected animals, analysis of cell populations by fluorescence-activated cell sorter (FACS) analysis, and fluorescence microscopy; 4) to examine the distribution of host cells (astrocytes and $C11b^+$ cells) inside and around both tumor models; and, finally, 5) to see if the uptake of CLIO-Cy5.5 by tumor and $CD11b^+$ cells observed with the 9L tumor occurred with other primary and metastatic brain tumor models. CD11b is expressed on both endogenously activated microglia and exogenous host cells such as macrophages [14] and is thus a useful marker of host response to tumors in the brain. We find that, with the 9L tumor implanted in nude mouse or rat hosts, CLIO-Cy5.5 was effective at delineating tumor margins due to its internalization by both tumor and $CD11b^+$ cells. The nanoparticle was internalized both by tumor and host cells in a model of brain metastasis using a mouse colon tumor line (CT26) and a second primary brain tumor model (Gli36 glioma).

Materials and Methods

Cell Culture

Rat 9L gliosarcoma and human Gli36 glioblastoma cell lines that were stably transfected to express GFP [15,16], as well as the 9L parent cell line from the American Type Culture Collection (ATCC; Manassas, VA), were cultured in DMEM supplemented with 10% fetal bovine serum (FBS), L-glutamine (2 mM), and penicillin (100 U/ml)/streptomycin (100 μg/ml). The mouse CT26 colon carcinoma cell line from ATCC was grown in RPMI 1640 supplemented with 10% FBS, L-glutamine (2 mM), penicillin (100 U/ml)/streptomycin (100 μg/ml), HEPES (10 mM) (Cambrex, Walkerville, MD), sodium pyruvate (1 mM), and 14 mM glucose. All cell lines were cultured at 37°C in a humidified 5% CO_2 atmosphere. Unless otherwise mentioned, products were from Cellgro (Herndon, VA).

Animal Models

Wistar male rats (200–250 g; Jackson Laboratory, Bar Harbor, ME), female nude mice (20–25 g, nu/nu, Cox-7, MGH, Boston, MA), and female GFP-expressing mice [20–25 g, FVB.Cg-Tg(GFPU)5Nagy/J; Jackson Laboratory] were anesthesized with isoflurane/O_2 and immobilized in a stereotactic frame. Tumor cell implantation in the brain was performed as previously described [6]. For mice, 4 μl of cell suspension containing 10^6 cells was injected 2 mm lateral to the bregma at a depth of 2 mm from the dural surface. The injection was performed slowly over 20 minutes, and the needle was withdrawn over another 2 minutes. For rats, the injection was performed over 15 minutes, and the needle was withdrawn over 2 minutes. The rat 9L GFP cell line was implanted in both rat and nude mouse brains. The mouse CT26 colon carcinoma was implanted in GFP-expressing mouse brain, and the human Gli36 GFP was implanted in nude mouse brain. For both rat and mouse, tumor cells were inoculated for 7 to 10 days.

MRI

Rat brain MRI studies were performed on a small animal Bruker 4.7-T Pharmascan magnet (Bruker, Billerica, MA) using a 38-mm-diameter rat head transmit–receive radiofrequency coil. Fast spin-echo axial T_1-weighted, T_2-weighted, and proton density images were acquired from the vertex to the skull base. All scans were acquired with a field of view = 3.5 cm, matrix size = 256 × 256, slice thickness = 0.8 mm, and NEX = 16. For T_1-weighted scans, T_E = 5.37 milliseconds and RARE factor = 4 for an effective T_E = 12.2 milliseconds, T_R = 500 milliseconds, and total acquisition time = 8 minutes 51 seconds. For T_2-weighted scans, T_E = 17.0 milliseconds and RARE factor = 8 for an effective T_E = 68.9 milliseconds, T_R = 2000 milliseconds, and total acquisition time = 18 minutes 9 seconds. For proton density scans, T_E = 5.37 milliseconds and RARE factor = 8 for an effective T_E = 21.8 milliseconds, T_R = 2000 milliseconds, and total acquisition time = 17 minutes 24 milliseconds. All images were acquired 24 hours after the administration of 15 mg/kg CLIO-Cy5.5 through tail vein injection. The superparamagnetic nanoparticle CLIO labeled with Cy5.5 was synthesized as previously described [6]. T_2-weighted images were acquired before the administration of Gd-DTPA, whereas T_1-weighted images were acquired after the intravenous administration of 0.3 mmol/kg Gd-DTPA (Magnevist; Schering, Berlin, Germany). The T_1-weighted images were thus acquired with both CLIO-Cy5.5 and Gd-DTPA present.

Optical Imaging

Animals were injected with 15 mg/kg CLIO-Cy5.5 through tail vein injection. Twenty-four hours after injection, anesthesized animals were slowly perfused with 100 ml of saline solution by inserting a large bore needle into the left ventricle

and by snipping the vena cava to allow the blood to leave the body. When appropriate, animals were further perfused with 100 ml of 4% paraformaldehyde (PFA; Fisher Scientific, Pittsburgh, PA) for tissue fixation. Craniotomy was performed to operatively remove the brain. Noninvasive optical imaging was performed as previously described [6]. Images of GFP, Cy5.5, and white light channels were acquired with an exposure time ranging from 100 to 800 milliseconds. Immediately after optical imaging, brains were frozen in an embedding medium (Sakura Finetek USA, Torrance, CA) and kept at −80°C, or tumors were isolated and disaggregated for flow cytometry.

Flow Cytometry for In Vivo *Uptake Evaluation*

After optical imaging, 9L tumors expressing GFP were isolated from non–PFA-fixed rat and nude mouse brains and further incubated with collagenase/dispase enzyme solution (Roche Diagnostics, Penzberg, Germany) for 1 hour at 37°C. When tumors had been entirely disaggregated, the cell suspensions was filtered and centrifuged on a density gradient of 44% Histopaque-1083 (Sigma, St. Louis, MO) HBSS. After aspiration of the supernatant, cell pellets were recovered and incubated for 1 hour at room temperature under agitation with R-phycoerythrin–labeled monoclonal mouse–anti-rat or rat–anti-mouse antibody CD11b for activated microglial and macrophage detection (used at 1 μl for 10^6 cells; Serotec, Oxford, UK). After antibody incubation, cells were washed with HBSS and incubated with 1% propidium iodide (PI; Molecular Probes, Eugene, OR) 1 minute before flow cytometry analysis to identify nonviable cells.

Immunohistochemistry and Fluorescent Microscopy

Frozen PFA-fixed and nonfixed brain from nude mice, GFP-expressing mice, and rats were cryosectioned into 20-μm-thick slices. For nonfixed tissue, brain sections were incubated for 5 minutes in PFA and washed twice in phosphate-buffered saline (PBS) before blocking. All sections were blocked with 10% normal goat serum (Jackson ImmunoResearch Laboratories, West Grove, PA) for 1 hour at room temperature. For glial fibrillary acidic protein (GFAP) immunolabeling, 0.3% Triton X-100 was added to the serum solution for plasma membrane permeabilization. After 1 hour, slides were washed thrice with PBS for 5 minutes each. After washing, brain sections were incubated with monoclonal mouse anti-rat or rat anti-mouse antibody CD11b (diluted 1/1000; Serotec) or polyclonal GFAP to detect astrocytes (diluted 1/500; DakoCytomation, Glostrup, Denmark). After 1 hour at room temperature, slices were washed with PBS thrice for 5 minutes each and then incubated with Cy3-conjugated goat anti-mouse or anti-rat antibodies for $CD11b^-$ and goat anti-rabbit for GFAP immunostaining (Jackson ImmunoResearch Laboratories; diluted 1/200). Secondary antibody solutions were complemented with 2% mouse or rat serum, depending on the animal tissue studied. After 1 hour at room temperature, slides were washed thrice with PBS for 5 minutes each and mounted in Vectashield mounting medium (Vector Laboratories, Burlingame, CA). Sections were immediately examined using an Eclipse 80i fluorescent microscope (Nikon, Melville, NY). Fluorescent images were captured with a forced-air–cooled CCD87 camera (Cascade 512B; Photometrics, Tucson, AZ). No labeling was visualized when the primary antibodies were omitted. In the case of CT26 and Gli36 cell lines implanted in GFP-expressing mouse and nude mouse, respectively, brain sections were observed without immunostaining. Frozen sections were directly mounted in Vectashield medium before image capture. For the study of CLIO-Cy5.5 uptake, the cell suspension was mounted on glass slides and immediately observed by fluorescent microscopy.

Determination of Tumor Delineation Using CLIO-Cy5.5

The 9L gliosarcoma cell line expressing GFP was implanted in nude mouse and rat brains. Nonfixed frozen tumors were entirely cryosectioned into 20-μm-thick coronal slices. For each animal model, six slices were selected from the center of the tumor, with a minimum distance of 50 μm between each slice. Four to five digital images of tumor and surrounding brain tissue were captured in both GFP and Cy5.5 channels for each slice using the fluorescent microscope described above. Using proprietary software developed by the authors (CMIR image, written using Interactive Data Language; Research Systems, Inc., Boulder, CO), the border of the tumors defined by GFP and Cy5.5 fluorescence was determined by calculating a threshold. The threshold corresponding to the mean between normal brain and tumor values for each slice was determined separately for GFP and Cy5.5, according to Eq. (1):

$$\text{Threshold} = B + 0.5(T - B) \quad (1)$$

where *B* is the pixel intensity of the background and *T* is the pixel intensity of the tumor. Specifically, an automated growing region-of-interest (ROI) algorithm was used, and the threshold was set at a value of 1/2 between the positive area (determined by the mean intensity of a circular ROI of tumor away from the border) and the negative area (determined by the mean intensity of a circular ROI of normal brain away from the tumor), with a boundary width of one pixel. Preset points on the *y*-axis were chosen (either at 1/2 of the distance from the top and bottom pixels or at 1/3 and 2/3 points) to minimize any bias in the analysis. A line was drawn from this point on the GFP demarcation line to the nearest point on the Cy5.5 line. All images for measurement were acquired at ×100 magnification, and measurement was calibrated by imaging a hemocytometer grid at the same magnification and by converting pixel values to micrometers. For each image, the distance between Cy5.5 and GFP borders was evaluated at two to three different predetermined positions, as detailed above, resulting in 66 and 65 margin measurements for nude mouse and rat, respectively. When the Cy5.5 border was found beyond the GFP border, we qualified the margin evaluation as an "overestimation." On the contrary, it was an "underestimation" when the GFP border was found beyond the Cy5.5 border. The values were plotted as a histogram, where the *x*-axis represents margin measurements organized in six equally spaced groups from the

smallest (greatest underestimation) to the highest values (greatest overestimation).

Results

Intraoperative Optical Imaging of the 9L Brain Tumor in Nude Mouse and Rat Hosts

The CLIO-Cy5.5 nanoparticle was previously demonstrated to act as a preoperative MRI and an intraoperative fluorescent contrast agent with a 9L GFP-expressing glioma tumor implanted in a rat [6]. To evaluate whether host response was an important variable in visualizing tumors with CLIO-Cy5.5 through fluorescence, we repeated the implantation in the rat brain, where it is known to be highly immunogenic [17], and in nude mice, which lack many facets of a normal immune response. Figure 1*A* shows a T_2-weighted image of an orthotopically implanted 9L tumor, which was taken 24 hours after CLIO-Cy5.5 administration, and a T_1-weighted image of the same slice after the addition of Gd-DTPA. The T_1 image reflects both possible T_1 enhancement by the CLIO-Cy5.5 and enhancement due to Gd-DTPA. Overall, the two images appear to delineate similar regions; however, on magnification (Figure 1*B*), the T_2-weighted nanoparticle image shows a more mottled appearance with notably dark regions at the border (white arrows). The T_2-weighted image suggests a higher intracellular accumulation of the CLIO-Cy5.5 at the tumor periphery compared with the tumor center, whereas tumor center accumulation is much higher than the adjacent brain. After craniotomy and removal of the brain, rat and nude mouse brains were imaged in white light, GFP, and Cy5.5 channels (Figure 1*C*). For both animal models, tumor delineation is clearly visualized by Cy5.5 fluorescence and is correlated with tumor extent as determined by GFP fluorescence. Further studies on the relationship between the GFP-defined tumor border and nanoparticle uptake evident by Cy5.5 fluorescence are described below.

Determination of the Cellular Uptake of Nanoparticles by Disaggregation and FACS

To determine the cellular uptake of CLIO-Cy5.5 *in vivo*, we performed flow cytometry on disaggregated tumor tissues from seven nude mice and seven rats with implanted 9L tumors that were injected with CLIO-Cy5.5. Only PI^- (live) cells were included in the analysis. As depicted in Figure 2*A*, we detected three cellular populations within the tumor: $CD11b^+$ cells, tumor cells (GFP^+), and a double-negative (DN) population without fluorescence (i.e., $CD11b^-$ and GFP^-). In nude mice, the percentage of tumor cells was approximately four-fold higher than that of $CD11b^+$ cells (Figure 2*B*). In rats, both cell types were in equal amounts, suggesting a greater immune response to the tumor in this model. The DN cells represent the major cellular population in both nude mouse and rat. However, this population also includes some tissues outside of the tumor, which was resected and included in the disaggregated suspension. The uptake of CLIO-Cy5.5 was determined for each population and was represented as histograms wherein uptake and events were illustrated in a logarithm scale (Figure 2*A*). In nude mouse and rat, both tumor cells and $CD11b^+$ cells, which together comprise the vast majority of uptake, showed

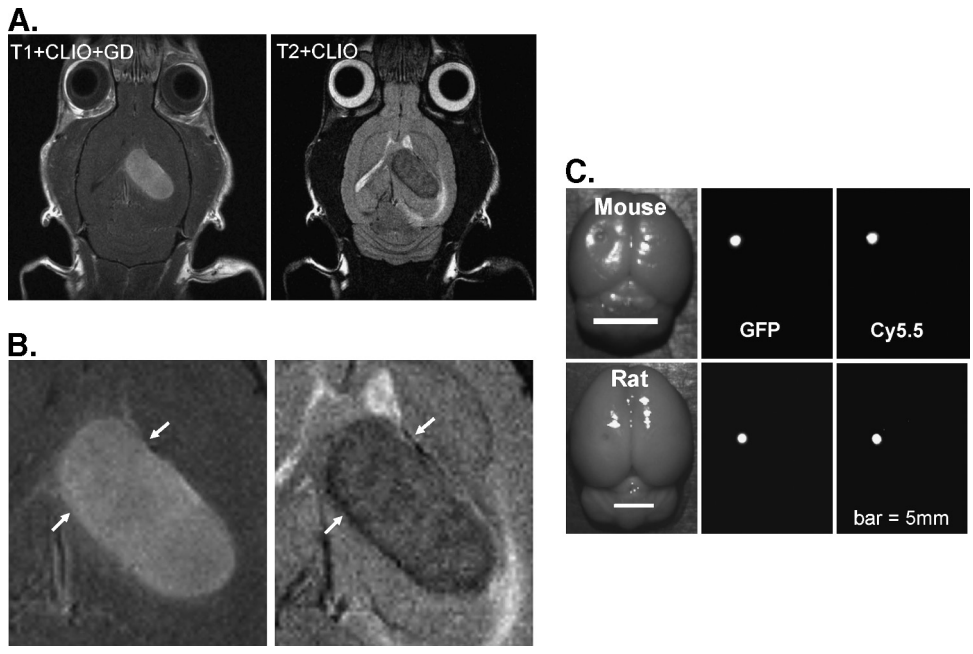

Figure 1. *CLIO-Cy5.5 nanoparticle as a preoperative MRI and as an intraoperative optical contrast agent. (A) A T_1-weighted image 10 minutes after gadolinium injection and 24 hours after CLIO-Cy5.5 injection, and an identically located T_2-weighted image in the same rat taken 24 hours after CLIO-Cy5.5 injection but before gadolinium injection. (B) Magnification of tumor region shown in (A), with arrows highlighting tumor borders. The CLIO-contrasted tumor is mottled, with a dark clearly defined margin on T_2-weighted imaging. (C). Optical images of mouse brain and rat brain after craniotomy. From left to right, the images are white light, GFP fluorescence, and CLIO-Cy5.5 fluorescence. Bar = 5 mm.*

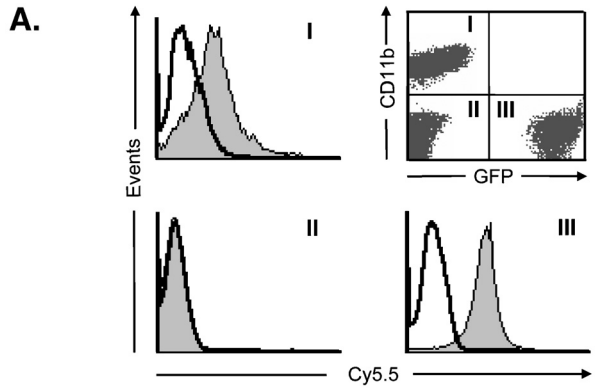

B.

	Percentage of cells (±SEM)		RMF Cy5.5 (±SEM)	
	Nude mouse	Rat	Nude mouse	Rat
CD11b+ cells (I)	4.28 ± 0.86	12.50 ± 3.07	3.94 ± 0.47	4.44 ± 1.10
DN cells (II)	78.79 ± 5.56	74.95 ± 6.61	1.03 ± 0.03	1.13 ± 0.06
Tumor cells (III)	15.85 ± 4.51	11.80 ± 3.73	5.90 ± 1.38	12.79 ± 2.69

Figure 2. *Flow cytometry of CLIO-Cy5.5 in cells from the 9L gliosarcoma. (A) A tumor-bearing animal was sacrificed 24 hours after injection with CLIO-Cy5.5, and the tumor was dissected and disaggregated. A dot plot showing three distinct cell populations is shown in the upper right panel. Populations were as follows: $CD11b^+/GFP^-$ (I); $CD11b^-/GFP^-$, DN, (II); and $CD11b^-/GFP^+$ (III). The uptake of CLIO-Cy5.5 as Cy5.5 fluorescence was analyzed in each of the three populations that are evident on the dot plot. $CD11b^+$ (I) and GFP^+ (III) cells internalized the nanoparticle as illustrated by the shift of the peaks. However, the DN population did not take up CLIO-Cy5.5. (B) The percentages of cells (left) and the relative median fluorescence (CLIO-Cy5.5 uptake; right) are given for each population of cells in both animal models.*

CLIO-Cy5.5 uptake; no CLIO-Cy5.5 uptake was observed in the DN population (Figure 2*B*).

Subsequently, the intracellular distribution of CLIO-Cy5.5 inside $CD11b^+$ and tumor cells was studied by microscopy using disaggregated cells. As depicted in Figure 3, the fluorescence of the nanoparticle was colocalized with the fluorescence of both tumor and $CD11b^+$ cells, validating FACS data and demonstrating *in vivo* the uptake of the nanoparticle by tumor cells and host cells from the tumor. The distribution of the nanoparticle within the cells was cytoplasmic and vesicular, suggesting endocytosis as the uptake mechanism of CLIO-Cy5.5.

Accuracy of Tumor Margin Determination and Spatial Localization of Activated Microglia/Macrophages and Astrocytes

The margins using tumor fluorescence (GFP fluorescence) and CLIO-Cy5.5 nanoparticle fluorescence (Cy5.5 fluorescence) were compared, as shown in Figure 4. Figure 4*A* illustrates an example tumor border in green and a nanoparticle border in red. The margin between the two borders was calculated over 130 measurements as described above and is represented in Figure 4, *B* and *C*. The average overestimation of the CLIO-Cy5.5 border compared to that of the GFP border was approximately 0.02 mm in the rat and 0.002 mm in the nude mouse, showing good similarity between the two species. The data depicted in Figure 4, *B* and *C*, were highly reproducible and show a high degree of accuracy, demonstrating the potential for precise intraoperative optical tumor margin determination in conditions of varying immune responses. When looking at the distribution of CLIO-Cy5.5 and $CD11b^+$ cells within the tumor, colocalization of both fluorescent signals was found at the periphery of the tumor (Figure 4*D*). In addition, the $CD11b^+$ cells infiltrated the tumor and colocalized with the nanoparticle inside the tumor. No CLIO-Cy5.5 was found in normal brain tissue. The minimal overestimation of the CLIO-Cy5.5 border, compared to the GFP border, could thus be explained by uptake of the nanoparticle inside activated microglia/macrophages at the periphery of the tumor. Inside the tumor, both the $CD11b^+$ cells and the tumor cells internalized the nanoparticle. The 0.018-mm difference in mean margin measurement between the nude mouse and the rat could be explained by the higher immune response found by flow cytometry analysis in the rat model. There were more activated microglia/macrophages at the periphery of the tumor in the case of the rat model.

In both animal models, the $CD11b^+$ cells showed a heterogeneous distribution with a very low level in normal brain, a medium level in the central portion of the tumor, and a high level at the periphery (Figure 5, *A* and *B*). In contradiction, astrocytes were found only beyond the tumor border, and no infiltration was detected inside the tumor (Figure 5, *C*–*F*). Moreover, as shown in Figure 5*C*, no colocalization of CLIO-Cy5.5 and GFAP signal could be found, suggesting no uptake of the nanoparticle by astrocytes.

Cellular Internalization of CLIO-Cy5.5 in a Model of Brain Metastasis and in a Second Primary Brain Tumor Model

As a metastasis brain tumor model, we chose the mouse CT26 colon carcinoma cell line. The nonfluorescent cell line was implanted inside the brain of GFP-expressing mice, allowing us to detect host cells by GFP fluorescence. As

shown in Figure 6*A*, CLIO-Cy5.5 was found in both host cells and tumor cells. Host cells mainly colocalized with CLIO-Cy5.5 at the periphery of the tumor, with some host cells infiltrating the tumor and showing colocalization with CLIO-Cy5.5. Arrowheads pointed to a clear uptake of the nanoparticle inside the host cells. The shape of the host cells was very similar to that of the $CD11b^+$ cells found in the 9L model, suggesting that activated microglia/macrophages infiltrated the CT26 tumor, as in the primary brain tumor model. Nanoparticles found inside the tumor but not colocalized with the GFP^+ host cells were internalized by intrinsically nonfluorescent tumor cells.

As a second model for primary brain tumor, we chose the glioblastoma cell line Gli36 expressing GFP. As shown in Figure 6*B*, CLIO-Cy5.5 colocalized with the GFP fluorescence expressed by tumor cells, demonstrating tumor cell uptake of the nanoparticle. The CLIO-Cy5.5 that did not colocalize with tumor cells was likely internalized by activated microglia/macrophages, as in the 9L case. In addition, Figure 6*C* shows in the center of a 9L tumor uptake of CLIO-Cy5.5 inside both tumor cells (arrow heads) and $CD11b^+$ cells (arrow). CLIO-Cy5.5 nanoparticle uptake by tumor and $CD11b^+$ cells occurred in both models, suggesting that nanoparticle uptake may provide an accurate method of margin delineation in these models as it does on 9L-based models.

Discussion

The similarity of MION and CLIO-Cy5.5 nanoparticles, and the history of use of MION to visualize brain tumors provide a unique rationale for studying the CLIO-Cy5.5 nanoparticle as an intraoperative margin-delineating agent. The MION nanoparticle has been used for brain tumor visualization with preclinical models [18–20] and with clinical studies in multiple centers [7,21,22]. As is shown in Figure 1 and as demonstrated by the literature, MION and CLIO-Cy5.5 uptake occurs with brain tumors and can be visualized by MRI. In addition, MION and CLIO-Cy5.5 nanoparticles have similar physical and biologic properties that include similar sizes, magnetic properties, blood half-lives, and biodistributions [9].

The studies performed here extend our earlier studies using CLIO-Cy5.5 for tumor margin delineation in a number of important directions [6].

Immune Response

To explore whether host immune response might play a role in nanoparticle uptake, we employed 9L gliosarcoma in rats, which developed a strong immune response to the tumor, and in immunocompromised nude mice. By FACS data with disaggregated tumor tissue, a higher percentage of $CD11b^+$ cells internalized the nanoparticle (Figure 2*B*) in the rat, and there was a slightly greater overestimation of the margins with the rat than with the mouse (Figure 4*B*). However, with both hosts, both CD11b and tumor cells internalized nanoparticles.

Method and Accuracy of Margin Estimation

Unlike earlier studies, a method of margin estimation using predefined thresholds was employed, and the magnification used for examining the margins was increased from 20-fold [6] (the whole tumor section was visualized) to 100-fold. Predefined thresholds and locations for margin determination were used to remove the possibility of any bias in selecting borders and allowed for a greater number of sampled

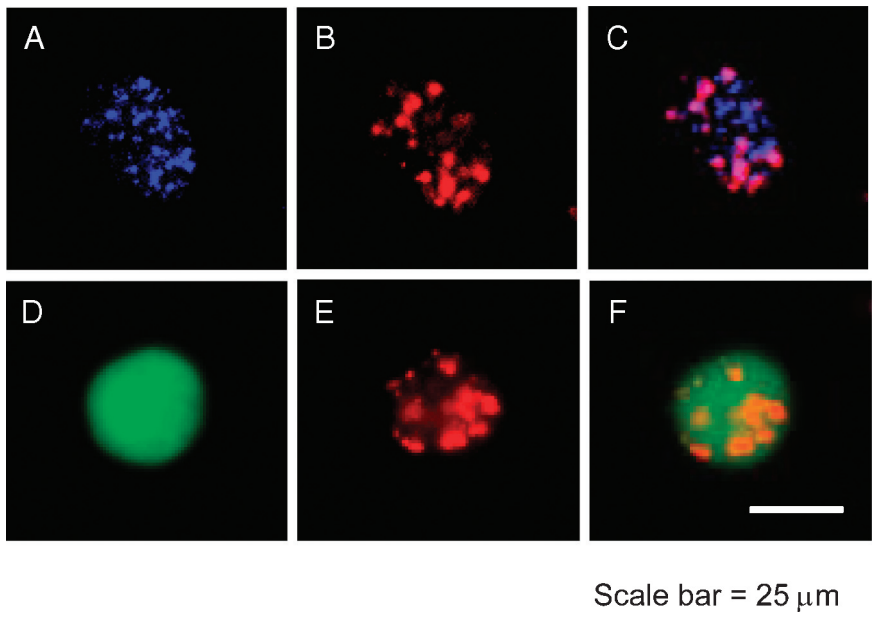

Figure 3. *CLIO-Cy5.5 uptake in cells from the 9L gliosarcoma. Activated microglia/macrophages were detected with R-phycoerythrin–labeled anti-CD11b (blue) in the rat host. Cells were disaggregated from intact tumors 24 hours after intravenous administration of CLIO-Cy5.5. For a $CD11b^+$ disaggregated cell, CD11b fluorescence (blue; A), CLIO-Cy5.5 fluorescence (red; B), and a merged image (C) are shown. For a GFP^+ disaggregated cell, GFP fluorescence (green; D), CLIO-Cy5.5 fluorescence (E), and a merged image (F) are shown. The nanoparticle appears to be in cytoplasmic vesicles within disaggregated cells and is in both tumor and $CD11b^+$ cells. Bar = 25 μm.*

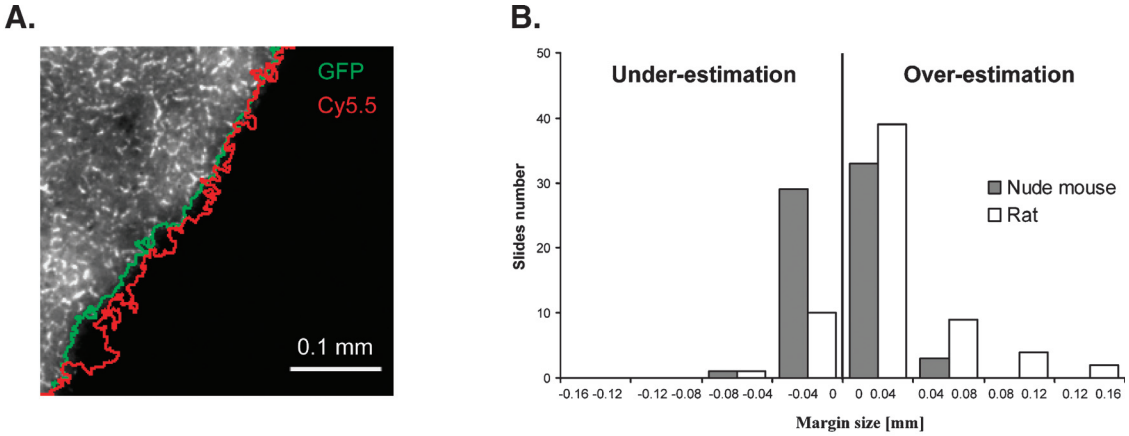

C.

	Nude mouse	Rat
Mean over-estimation [mm]	0.002	0.024
SD [mm]	0.02	0.038
SEM [mm]	0.002	0.005
Max over-estimation [mm]	0.065	0.151
Max under-estimation [mm]	-0.064	-0.057

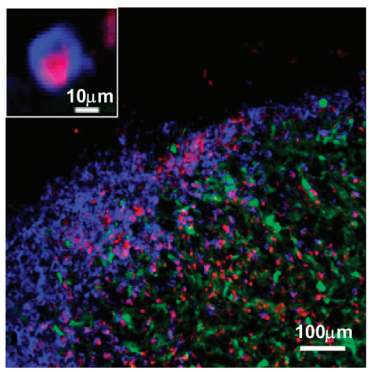

Figure 4. *Tumor border determination using CLIO-Cy5.5. (A) Tumor border determined using signal intensity measurements. The border was determined using Eq. 1 (9L gliosarcoma/nude mouse host) based on GFP fluorescence (green boundary) or CLIO-Cy5.5 fluorescence (red boundary). GFP fluorescence is shown in gray. (B) Accuracy of tumor border by CLIO-Cy5.5 fluorescence. The Cy5.5 border extension beyond the GFP border is defined as overestimation; the reverse is defined as underestimation. The majority of measurements between the two borders were close to zero for both rat and nude mouse models. (C) Accuracy of border determination by CLIO-Cy5.5 fluorescence. The standard deviation (SD), standard error of the mean (SEM), maximum overestimation, and maximum underestimation are given. (D) Etiology of slight differences in margin determination between models. Fluorescent microscopy micrograph of a 20-μm-thick brain slice labeled with anti-CD11b antibody for microglia/macrophage staining (blue); tumor cells are in green, CLIO-Cy5.5 is in red, and normal brain is in black. (D) Inset: Accumulation of CLIO-Cy5.5 inside CD11b$^+$ cells (microglia/macrophages). The nanoparticle localizes at the periphery of the tumor inside microglia/macrophages and in the tumor inside tumor cells and microglia/macrophages. The slight overestimation in rat brains corresponds to the nanoparticle localized around the tumor inside microglia/macrophages.*

points. We found that the mean overestimation was 2 μm for 9L tumors in nude mice and was 24 μm in rats. Importantly, the maximum overestimation was 65 and 151 μm, respectively, and the maximum underestimation was 64 and 57 μm, respectively. This suggests that, even with full immune response, the tumor boundary reported was within a few cell diameters of the true boundary. Importantly for resection, the maximum underestimation was even less than the areas of slight overestimation. The fact that both tumor cells and host cells take up the particle helps prevent areas of gross underestimation due to focal lack of macrophages or activated microglia. This also suggests that the nanoparticle should be reported accurately in conditions in which the host response may be blunted, such as after chemotherapy.

Determination of Cells Internalizing CLIO-Cy5.5 by Disaggregation and FACS

To determine the cells internalizing the nanoparticle, we supplemented fluorescence microscopy on tissue sections with tumor disaggregation followed by the determination of cell fluorescence using FACS. To our knowledge, this is the first time that such an analysis has been applied to determine nanoparticle uptake in brain tumor models. In both the nude mouse and the rat, three cellular populations were seen: tumor cells, activated microglia/macrophages, and a distinct third population. Microglia are known to be a major component of the central nervous system (CNS) immune response participating in the CNS response to several neurologic disorders, including tumors [23]. On activation, those cells change their physiologic and morphologic properties and increase their phagocytic capacities [24]. In addition, some studies showed a significant increase in the percentage of macrophages and microglia within malignant gliomas, rising up to 50% of the tumor area [25,26]. Interestingly, normal mouse and rat brains show no CD11b$^+$ cells or diffuse expression of CD11b antigen (Tréhin et al., unpublished observations).

Distribution of Host Cells within Tumors

By fluorescent microscopy, we analyzed the distribution of different cellular populations within the 9L tumor in both the rat and the mouse hosts. CD11b$^+$ microglia/macrophages

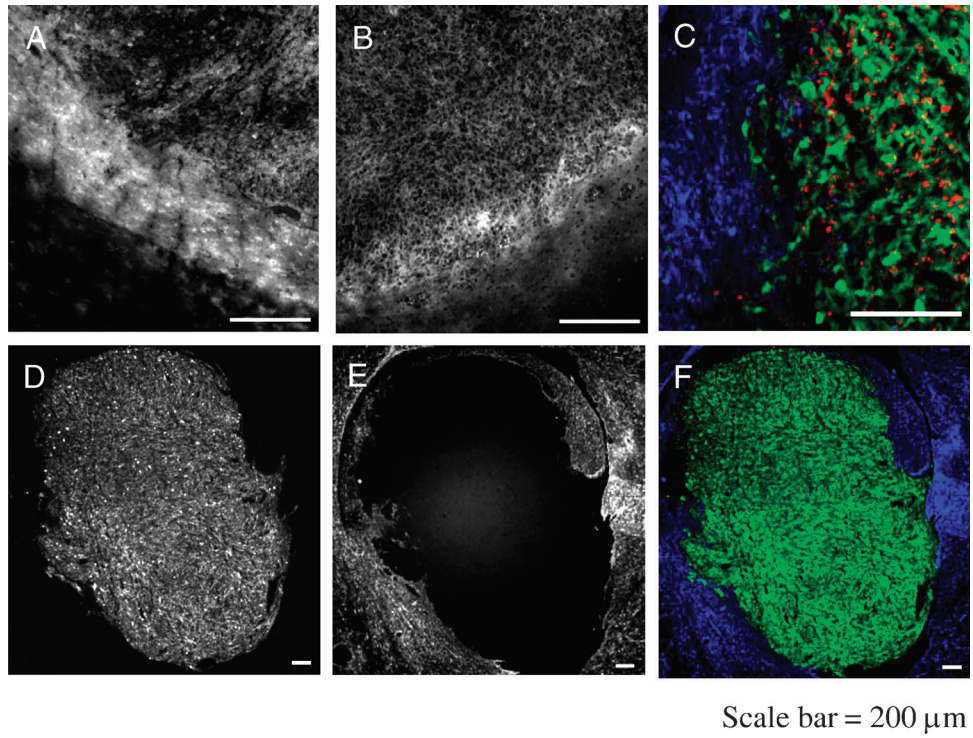

Figure 5. *Distribution of microglia/macrophages and astrocytes with the 9L gliosarcoma. (A) Fluorescence from anti-CD11b antibody stain (microglia/macrophages) in the rat. (B) Fluorescence from anti-CD11b antibody stain in the nude mouse. CD11b$^+$ cells form a ring-like pattern around the tumor that is more pronounced in the rat than in the nude mouse. (C) Tumor margin in the rat host after staining with anti-GFAP, a marker of astrocytes. Astrocytes are in blue, CLIO-Cy5.5 is in red, and tumor GFP is in green. Astrocytes lack CLIO-Cy5.5 and are not present in the tumor. (D) Tumor GFP fluorescence at low magnification. (E) Anti-GFAP fluorescence of astrocytes at low magnification. The antibody was Cy3-labeled. (F) Color merge of (D) and (E). Astrocytes do not centrally infiltrate brain tumor and do not internalize CLIO-Cy5.5. Bar = 200 μm.*

were mostly located at the periphery of the tumor, forming a ring-like pattern around the tumor (Figures 4*D* and 5, *A* and *B*). However, occasional CD11b$^+$ cells were seen throughout the tumor (Figures 4*D* Figures 5, *A* and *B*, Figures 6*C*). This distribution may be explained by increased vascularity peripherally relative to the tumor center and reflects a pattern of macrophage infiltration [27,28]. By immunohistochemistry, GFAP$^+$ cells (astrocytes) did not internalize CLIO-Cy5.5 (Figure 5, *C*–*F*)—an observation consistent with the high percentage of GFP$^-$ CD11b$^-$ cells obtained with flow cytometry data on disaggregated tumors (Figure 2*B*).

Cellular Internalization of CLIO-Cy5.5 in Different Brain Tumor Models

We found that the CLIO-Cy5.5 nanoparticle was internalized by both CD11b$^+$ cells and tumor cells in four animal

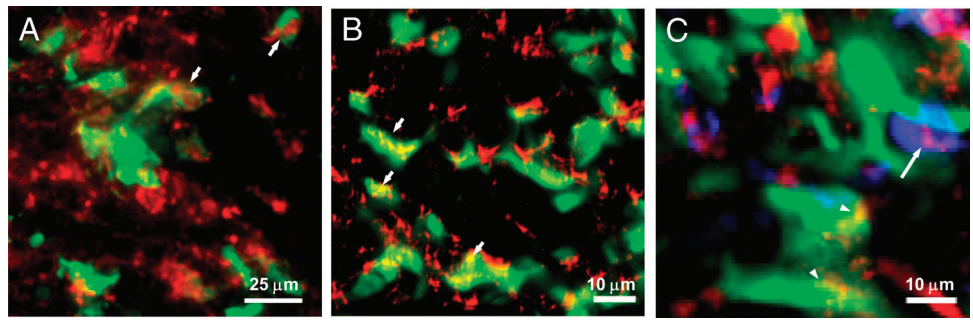

Figure 6. *CLIO-Cy5.5 uptake by tumor and host cells in primary and metastatic tumor models. (A) Nonfluorescent CT26 colon carcinoma implanted in GFP-expressing mouse, injected with CLIO-Cy5.5, and imaged. CLIO-Cy5.5 (red) is found in GFP (green)–expressing cells (host) and in regions of no GFP (tumor cells). (B) Gli36 GFP tumor (green) shows CLIO-Cy5.5 fluorescence (red) associated with GFP, demonstrating tumoral uptake. CLIO-Cy5.5 nanoparticles that do not colocalize with tumor cells are in CD11b$^+$ cells. (C) The center of the 9L tumor expressing GFP. Tumor cells are in green, CLIO-Cy5.5 is in red, and microglia/macrophages are in blue. The arrow points to the colocalization of the CLIO-Cy5.5 with microglia/macrophages, and arrowheads point to colocalization with tumor cells.*

models. They were the 9L gliosarcoma in the rat host, the 9L tumor in the nude mouse host, the CT26 colon carcinoma implanted in a GFP-expressing mouse, and a human Gli36 tumor implanted in a nude mouse.

The cellular disposition of magnetic nanoparticles in brain tumors has been examined by different groups with somewhat different conclusions. Uptake by microglia/macrophages has been seen in animal models [20] and in clinical studies [7,22]. However, uptake by tumor cells has been noted in other animal models [15,18,19]. The contrasting observations may be explained by the use of techniques of varying sensitivity and specificity to detect the presence of nanoparticles. Detection of nanoparticles with clinical samples, and in many animal studies as well, relies on iron staining that detects both injected and endogenous iron. In contrast, the background fluorescence used in detecting the Cy5.5 fluorescence of the nanoparticle is essentially zero because the brain has no naturally occurring materials that fluoresce in the near-infrared region of the spectrum. Fluorescent microscopy easily detects small populations of cells that have high concentrations of label, but has difficulty distinguishing small amounts of label present in a high percentage of cells from background fluorescence. For that reason, we employed tissue disaggregation, followed by quantitation of cell-associated label by FACS, as a method of detecting fluorescence in different populations of cells. After obtaining similar results with disaggregation/FACS and fluorescence microscopy in two 9L-related models, we employed fluorescence microscopy to examine nanoparticle distribution in two additional animal models. Our conclusion that nanoparticle uptake occurs both in tumor and in host cells is supported by multiple techniques and multiple animal models.

The tumor models we employed featured relatively definitive margins, in comparison to clinical versions of glioblastoma multiforme, which are highly infiltrative. However, the models we selected were adequate to attain the major goals of the study, which were to characterize the 9L model with respect to the cellular basis of nanoparticle uptake using an improved FACS-based quantitation, to apply that technology in different tumor cell lines and different hosts, and to develop a reader-independent accurate methodology for margin delineation. Based on the results of the current study, the use of magneto-optical nanoparticles for margin determination might be successfully extended to ectopic rodent brain tumor models using cell lines that have demonstrated highly infiltrative behavior and/or micrometastases similar to those seen in human brain cancer. These include RT2 glioma [29,30], C6 glioblastoma [31,32], and F98 glioma [17,33]. Moreover, the generally grim outlook for brain cancer patients due to tumor cell dissemination has not prevented either resection as treatment or efforts to improve resection technique by providing the surgeon with nonvisible light-based sources of information on which to base decisions. Techniques investigated for their ability to provide intraoperative information, in addition to our own approach using magneto-optical nanoparticles, include intraoperative MRI [34,35], intraoperative ultrasound [36,37], and intraoperative fluorescence from probes including porphyrins, [38,39], indocyanine green [5], fluorescein [40], and fluorescein–albumin [41].

In conclusion, with the 9L model, we demonstrated that the CLIO-Cy5.5 nanoparticle accurately delineates tumor margins by localizing inside tumor cells and microglia/macrophages, with no uptake detected in other cell types. Similar results were obtained with both immunodeficient and immunocompetent hosts. A pattern of combined tumor cell and host cell uptake was seen in a glioblastoma primary tumor (Gli36) and in a colon carcinoma metastatic tumor model (CT26). The techniques developed here to assess the accuracy of margin determination and to identify the cells internalizing nanoparticles can be applied to a wider variety of animal brain tumor models, in an effort to understand more fully the value of developing a fluorescent nanoparticle that is suitable for clinical use as an intraoperative contrast agent for tumor delineation.

References

[1] Winger MJ, Macdonald DR, and Cairncross JG (1989). Supratentorial anaplastic gliomas in adults. The prognostic importance of extent of resection and prior low-grade glioma. *J Neurosurg* **71,** 487–493.

[2] Bucci MK, Maity A, Janss AJ, Belasco JB, Fisher MJ, Tochner ZA, Rorke L, Sutton LN, Phillips PC, and Shu HK (2004). Near complete surgical resection predicts a favorable outcome in pediatric patients with nonbrainstem, malignant gliomas: results from a single center in the magnetic resonance imaging era. *Cancer* **101,** 817–824.

[3] Moore GE (1947). Fluorescein as an agent in the differentiation of normal and malignant tissues. *Science* **106,** 130–131.

[4] Haglund MM, Hochman DW, Spence AM, and Berger MS (1994). Enhanced optical imaging of rat gliomas and tumor margins. *Neurosurgery* **35,** 930–940 (discussion 940–931).

[5] Haglund MM, Berger MS, and Hochman DW (1996). Enhanced optical imaging of human gliomas and tumor margins. *Neurosurgery* **38,** 308–317.

[6] Kircher MF, Mahmood U, King RS, Weissleder R, and Josephson L (2003). A multimodal nanoparticle for preoperative magnetic resonance imaging and intraoperative optical brain tumor delineation. *Cancer Res* **63,** 8122–8125.

[7] Varallyay P, Nesbit G, Muldoon LL, Nixon RR, Delashaw J, Cohen JI, Petrillo A, Rink D, and Neuwelt EA (2002). Comparison of two superparamagnetic viral-sized iron oxide particles ferumoxides and ferumoxtran-10 with a gadolinium chelate in imaging intracranial tumors. *AJNR Am J Neuroradiol* **23,** 510–519.

[8] McLachlan SJ, Morris MR, Lucas MA, Fisco RA, Eakins MN, Fowler DR, Scheetz RB, and Olukotun AY (1994). Phase I clinical evaluation of a new iron oxide MR contrast agent. *J Magn Reson Imaging* **4,** 301–307.

[9] Wunderbaldinger P, Josephson L, Bremer C, Moore A, and Weissleder R (2002). Detection of lymph node metastases by contrast-enhanced MRI in an experimental model. *Magn Reson Med* **47,** 292–297.

[10] Saleh A, Schroeter M, Jonkmanns C, Hartung HP, Modder U, and Jander S (2004). *In vivo* MRI of brain inflammation in human ischaemic stroke. *Brain* **127,** 1670–1677.

[11] Weissleder R, Stark DD, Engelstad BL, Bacon BR, Compton CC, White DL, Jacobs P, and Lewis J (1989). Superparamagnetic iron oxide: pharmacokinetics and toxicity. *AJR Am J Roentgenol* **152,** 167–173.

[12] Weissleder R and Ntziachristos V (2003). Shedding light onto live molecular targets. *Nat Med* **9,** 123–128.

[13] Funovics MA, Weissleder R, and Mahmood U (2004). Catheter-based *in vivo* imaging of enzyme activity and gene expression: feasibility study in mice. *Radiology* **231,** 659–666.

[14] Wirenfeldt M, Babcock AA, Ladeby R, Lambertsen KL, Dagnaes-Hansen F, Leslie RG, Owens T, and Finsen B (2005). Reactive microgliosis engages distinct responses by microglial subpopulations after minor central nervous system injury. *J Neurosci Res* **82,** 507–514.

[15] Moore A, Marecos E, Bogdanov A Jr, and Weissleder R (2000). Tumoral distribution of long-circulating dextran-coated iron oxide nanoparticles in a rodent model. *Radiology* **214,** 568–574.

[16] Shah K, Bureau E, Kim DE, Yang K, Tang Y, Weissleder R, and Breakefield XO (2005). Glioma therapy and real-time imaging of neural precursor cell migration and tumor regression. *Ann Neurol* **57,** 34–41.
[17] Barth RF (1998). Rat brain tumor models in experimental neuro-oncology: the 9L, C6, T9, F98, RG2 (D74), RT-2 and CNS-1 gliomas. *J Neuro-Oncol* **36,** 91–102.
[18] Zimmer C, Weissleder R, Poss K, Bogdanova A, Wright SC Jr, and Enochs WS (1995). MR imaging of phagocytosis in experimental gliomas. *Radiology* **197,** 533–538.
[19] Zimmer C, Wright SC Jr, Engelhardt RT, Johnson GA, Kramm C, Breakefield XO, and Weissleder R (1997). Tumor cell endocytosis imaging facilitates delineation of the glioma–brain interface. *Exp Neurol* **143,** 61–69.
[20] Fleige G, Nolte C, Synowitz M, Seeberger F, Kettenmann H, and Zimmer C (2001). Magnetic labeling of activated microglia in experimental gliomas. *Neoplasia* **3,** 489–499.
[21] Enochs WS, Harsh G, Hochberg F, and Weissleder R (1999). Improved delineation of human brain tumors on MR images using a long-circulating, superparamagnetic iron oxide agent. *J Magn Reson Imaging* **9,** 228–232.
[22] Neuwelt EA, Varallyay P, Bago AG, Muldoon LL, Nesbit G, and Nixon R (2004). Imaging of iron oxide nanoparticles by MR and light microscopy in patients with malignant brain tumours. *Neuropathol Appl Neurobiol* **30,** 456–471.
[23] Streit WJ (2000). Microglial response to brain injury: a brief synopsis. *Toxicol Pathol* **28,** 28–30.
[24] Streit WJ and Kincaid-Colton CA (1995). The brain's immune system. *Sci Am* **273,** 54–55, 58–61.
[25] Roggendorf W, Strupp S, and Paulus W (1996). Distribution and characterization of microglia/macrophages in human brain tumors. *Acta Neuropathol (Berl)* **92,** 288–293.
[26] Badie B and Schartner JM (2000). Flow cytometric characterization of tumor-associated macrophages in experimental gliomas. *Neurosurgery* **46,** 957–961 (discussion 961–952).
[27] Morioka T, Baba T, Black KL, and Streit WJ (1992). Response of microglial cells to experimental rat glioma. *Glia* **6,** 75–79.
[28] Morioka T, Baba T, Black KL, and Streit WJ (1992). Immunophenotypic analysis of infiltrating leukocytes and microglia in an experimental rat glioma. *Acta Neuropathol (Berl)* **83,** 590–597.
[29] Fillmore HL, Shurm J, Furqueron P, Prabhu SS, Gillies GT, and Broaddus WC (1999). An *in vivo* rat model for visualizing glioma tumor cell invasion using stable persistent expression of the green fluorescent protein. *Cancer Lett* **141,** 9–19.
[30] Mourad PD, Farrell L, Stamps LD, Santiago P, Fillmore HL, Broaddus WC, and Silbergeld DL (2003). Quantitative assessment of glioblastoma invasion *in vivo*. *Cancer Lett* **192,** 97–107.
[31] Chicoine MR and Silbergeld DL (1995). Invading C6 glioma cells maintaining tumorigenicity. *J Neurosurg* **83,** 665–671.
[32] Grobben B, De Deyn PP, and Slegers H (2002). Rat C6 glioma as experimental model system for the study of glioblastoma growth and invasion. *Cell Tissue Res* **310,** 257–270.
[33] Kobayashi N, Allen N, Clendenon NR, and Ko LW (1980). An improved rat brain-tumor model. *J Neurosurg* **53,** 808–815.
[34] Nimsky C, Ganslandt O, Von Keller B, Romstock J, and Fahlbusch R (2004). Intraoperative high-field-strength MR imaging: implementation and experience in 200 patients. *Radiology* **233,** 67–78.
[35] Fenchel S, Boll DT, and Lewin JS (2003). Intraoperative MR imaging. *Magn Reson Imaging Clin North Am* **11,** 431–447.
[36] Renner C, Lindner D, Schneider JP, and Meixensberger J (2005). Evaluation of intra-operative ultrasound imaging in brain tumor resection: a prospective study. *Neurol Res* **27,** 351–357.
[37] Unsgaard G, Ommedal S, Muller T, Gronningsaeter A, and Nagelhus Hernes TA (2002). Neuronavigation by intraoperative three-dimensional ultrasound: initial experience during brain tumor resection. *Neurosurgery* **50,** 804–812 (discussion 812).
[38] Stummer W, Reulen HJ, Novotny A, Stepp H, and Tonn JC (2003). Fluorescence-guided resections of malignant gliomas—an overview. *Acta Neurochir Suppl* **88,** 9–12.
[39] Stummer W, Stocker S, Wagner S, Stepp H, Fritsch C, Goetz C, Goetz AE, Kiefmann R, and Reulen HJ (1998). Intraoperative detection of malignant gliomas by 5-aminolevulinic acid–induced porphyrin fluorescence. *Neurosurgery* **42,** 518–525 (discussion 525–516).
[40] Kabuto M, Kubota T, Kobayashi H, Nakagawa T, Ishii H, Takeuchi H, Kitai R, and Kodera T (1997). Experimental and clinical study of detection of glioma at surgery using fluorescent imaging by a surgical microscope after fluorescein administration. *Neurol Res* **19,** 9–16.
[41] Kremer P, Wunder A, Sinn H, Haase T, Rheinwald M, Zillmann U, Albert FK, and Kunze S (2000). Laser-induced fluorescence detection of malignant gliomas using fluorescein-labeled serum albumin: experimental and preliminary clinical results. *Neurol Res* **22,** 481–489.